STABILITY OF AN ELASTIC ROD BUCKLING INTO A SOFT WALL

ROBERT S. MANNING* AND GEORGE B. BULMAN†

Abstract. The conjugate point theory of the calculus of variations is extended to apply to the buckling of an elastic rod in an external field, using the operator approach presented in [14], which we show can be used when the second variation operator is an integrodifferential operator, rather than a differential operator as in the classical case. The external field is chosen to model two parallel "soft" walls. We consider the examples of 2D buckling under both pinned-pinned and clamped-clamped boundary conditions, as well as the 3D clamped-clamped problem, where we consider the importance of the rod cross-section shape as it ranges from circular to extreme elliptical. For each of these problems, we find that in the appropriate limit, the soft-wall solutions approach a "hard-wall" limit, and so we make conjectures about these hard-wall contact equilibria and their stability. In the 2D pinned-pinned case, this allows us to assign stability to the configurations reported in [9] and reconsider the experimental results discussed therein.

Key words. conjugate points, stability, index, elastic rod, buckling, wall contact

AMS subject classifications. 49K22, 74G60, 74K10

1. Introduction. In the classical theory of the calculus of variations, the stability of an equilibrium of a functional is investigated by searching for conjugate points using the Euler-Jacobi equation [7]. In a refinement due to Morse [15], the number of conjugate points is seen to be a stability index giving the dimension of the space of allowed variations that lower the energy. Here we follow the functional analytic approach of [14] to this classical problem in order to extend the stability theory to the case of an elastic rod buckling in an external field. The standard Euler-Jacobi theory does not apply to this problem, as the second variation operator is an integrodifferential operator.

The standard problem of interest is to find critical points (equilibria) of a functional

$$E[\mathbf{q}] = \int_0^1 L(\mathbf{q}'(s), \mathbf{q}(s), s) ds$$

subject to the conditions $\mathbf{q}(0) = \mathbf{q}_i$, $\mathbf{q}(1) = \mathbf{q}_f$. Equilibria satisfy the Euler-Lagrange equation

$$\frac{d}{ds}\left(\frac{\partial L}{\partial \mathbf{q}'}\right) = \frac{\partial L}{\partial \mathbf{q}}.$$

Stability is determined by analyzing the second variation of E, which is conveniently written in the form

$$\delta^2 E[\boldsymbol{\zeta}] = \int_0^1 \boldsymbol{\zeta}(s)^T (\mathcal{S}\boldsymbol{\zeta})(s)\, ds,$$

where $\mathcal{S}$ is a second-order differential operator, and $\boldsymbol{\zeta}$ is an allowed variation in $\mathbf{q}$, which must satisfy $\boldsymbol{\zeta}(0) = \boldsymbol{\zeta}(1) = \mathbf{0}$. A condition for stability is then that the equilibrium have no conjugate point, where a conjugate point is defined to be a value $\sigma < 1$ for which the Euler-Jacobi equation $\mathcal{S}\boldsymbol{\zeta} = \mathbf{0}$ has a solution $\boldsymbol{\zeta}$ (not identically zero) with $\boldsymbol{\zeta}(0) = \boldsymbol{\zeta}(\sigma) = \mathbf{0}$. If there are conjugate points, then their number is called the index, which gives the dimension of the space of allowed variations on which the second variation $\delta^2 E$ is negative.

*Mathematics Department; Haverford College; Haverford, PA 19041 USA (rmanning@haverford.edu), Author to whom correspondence should be addressed.

†370 Lancaster Ave.; Haverford College; Haverford, PA 19041 USA (george_bulman@hotmail.com).

In [14], this theory is extended to give analogous conjugate point results for the case of an isoperimetrically constrained problem, with the only change that the second variation operator $\mathcal{S}$ is replaced by the operator $\mathcal{Q}\mathcal{S}\mathcal{Q}$, where $\mathcal{Q}$ is a projection onto the orthogonal complement of the linearized constraints. This theory is thus couched in functional analytic language, but the computation of conjugate points is easily translated into an initial value problem (IVP) for a system of ordinary differential equations; the unknowns in this IVP are assembled into a "stability matrix", and a conjugate point occurs when the determinant of this matrix vanishes.

Here, we show that this functional analytic approach can be used to extend the stability theory to problems not covered by the standard calculus of variations approach. In particular, we look at the example of a rod in an external field, where the second variation operator contains an integral operator term in addition to the second-order differential operator $\mathcal{S}$. Once a few basic spectral properties are proven for this operator, the theory from [14] immediately applies, and provides the definition of "conjugate point" appropriate to this problem. Furthermore, as in the isoperimetrically constrained example, the required computations to find conjugate points can be reduced to an IVP for a system of ordinary differential equations, despite the fact that the second variation contains an integral operator.

We illustrate this stability theory on several variants of the Euler buckling problem, in which one end of an intrinsically straight elastic rod is subjected to a compressive load λ. We consider both clamped-clamped and pinned-pinned boundary conditions, and we add the constraint that the only translational freedom of motion of the two ends is a compression toward each other. To this classic problem, we add an external field that models two parallel "soft" walls surrounding the rod. Each wall exerts a repulsive force on each infinitesimal segment of the rod, and this force increases to positive infinity as the segment's lateral displacement approaches a wall spacing parameter a. For sufficiently large λ, the rod can buckle into nontrivial equilibrium configurations, which are dependent on the strength of, and spacing between, the walls, as well as on the shape of the rod cross-section in 3-dimensional (3D) rods (we consider both circular and elliptical cross-sections).

Holmes, Domokos, and Hek [8] have considered a similar rod-in-a-field problem, for a 2D pinned-pinned rod in a quadratic potential, combining theoretical analysis of the equilibria via a dynamical systems perspective with extensive numerical simulations of the global bifurcation diagram using the parallel simplex algorithm. In contrast, our focus is on determining stability via the theory summarized above, which we illustrate on a small set of branches of equilibria computed using the parameter continuation package AUTO [5].

In addition, we may consider the hard-wall limit of our soft-wall potential as a means to impute stability properties to hard-wall equilibria, such as those computed in the 2D pinned-pinned case by Holmes et al [9]. As we show in Sec. 5.1, this stability information explains, among other things, the experimentally-observed hysteresis reported in [9]. A similar approach could, in principle, be used to determine the stability of equilibria in other "hard constraint" settings, such as the asymmetric

wall problem considered by Roman and Pocheau [18] or even more complicated geometries such as buckling on a cylinder, as considered recently by van der Heijden [20]. In addition to providing a useful tool for understanding hard constraints, one can also view the soft-wall problem considered here as an important step toward the development of a theory of stability for rod *self*-contact configurations, since a Debye-Huckel potential is a widely used model for the self-repulsion of DNA in supercoiled configurations.

2. Equilibrium equations for an elastic rod. Here we summarize the standard theory of inextensible and unshearable elastic rods [1, 4, 11, 12] and present the calculus of variations problem relevant for the buckling of such a rod in the presence of an external field with potential energy V. We begin with the full 3D theory, and then turn at the end of the section to the simpler 2D case.

The configuration of a rod is described by a centerline $\mathbf{r}(s) = (x(s), y(s), z(s))$ (written as a function of arclength s) and a set of directors $\{\mathbf{d}_1(s), \mathbf{d}_2(s), \mathbf{d}_3(s)\}$ that form an orthonormal frame giving the orientation of the cross-section of the rod at location s. We choose $\mathbf{d}_1$ to lie along one axis of the elliptical cross-section, $\mathbf{d}_2$ to lie along the other axis, and $\mathbf{d}_3$ to be orthogonal to the cross-section. For convenience, we choose a length scale so that $0 \le s \le 1$. Inextensibility and unshearability of the rod are imposed by requiring that $\mathbf{d}_3$ equals the tangent vector to the centerline, or, letting $'$ denote differentiation with respect to s:

$$\mathbf{r}'(s) = \mathbf{d}_3(s).$$

The bending and twisting energy of the rod is defined in terms of the *strains*:

$$u_1(\mathbf{d}_1, \mathbf{d}_2, \mathbf{d}_3) \equiv -\mathbf{d}_2^T \mathbf{d}_3', \quad u_2(\mathbf{d}_1, \mathbf{d}_2, \mathbf{d}_3) \equiv \mathbf{d}_1^T \mathbf{d}_3', \quad u_3(\mathbf{d}_1, \mathbf{d}_2, \mathbf{d}_3) \equiv \mathbf{d}_2^T \mathbf{d}_1'.$$

The directors and strains can be written as rational functions of Euler parameters $\mathbf{q} \in \mathbb{R}^4$:

$$\mathbf{d}_1 = \frac{1}{|\mathbf{q}|^2} \begin{bmatrix} q_1^2 - q_2^2 - q_3^2 + q_4^2 \\ 2q_1q_2 + 2q_3q_4 \\ 2q_1q_3 - 2q_2q_4 \end{bmatrix}, \; \mathbf{d}_2 = \frac{1}{|\mathbf{q}|^2} \begin{bmatrix} 2q_1q_2 - 2q_3q_4 \\ q_4^2 - q_1^2 + q_2^2 - q_3^2 \\ 2q_2q_3 + 2q_1q_4 \end{bmatrix}, \; \mathbf{d}_3 = \frac{1}{|\mathbf{q}|^2} \begin{bmatrix} 2q_1q_3 + 2q_2q_4 \\ 2q_2q_3 - 2q_1q_4 \\ q_4^2 - q_1^2 - q_2^2 + q_3^2 \end{bmatrix},$$

$$u_i = \frac{2\left(\mathbf{q}'\right)^T \mathbf{B}_i \mathbf{q}}{|\mathbf{q}|^2},$$

where

$$\mathbf{B}_1 = \begin{bmatrix} 0 & 0 & 0 & 1 \\ 0 & 0 & 1 & 0 \\ 0 & -1 & 0 & 0 \\ -1 & 0 & 0 & 0 \end{bmatrix}, \; \mathbf{B}_2 = \begin{bmatrix} 0 & 0 & -1 & 0 \\ 0 & 0 & 0 & 1 \\ 1 & 0 & 0 & 0 \\ 0 & -1 & 0 & 0 \end{bmatrix}, \; \mathbf{B}_3 = \begin{bmatrix} 0 & 1 & 0 & 0 \\ -1 & 0 & 0 & 0 \\ 0 & 0 & 0 & 1 \\ 0 & 0 & -1 & 0 \end{bmatrix}.$$

2.1. Energy. We make the common assumption that E depends quadratically on the strains, and add a potential energy term V:

$$E \equiv \int_0^1 \left[\frac{1}{2} \left(\sum_{i=1}^{3} K_i [u_i(\mathbf{q}'(s), \mathbf{q}(s))]^2 \right) + \lambda d_{33}(\mathbf{q}(s)) + V(\mathbf{r}(s)) \right] ds.$$

Here, K_i are the bending ($i = 1, 2$) and twisting ($i = 3$) stiffnesses of the rod, λ is the imposed load, and d_{33} is the z-component of the director $\mathbf{d}_3$. We let

$$V(\mathbf{r}) = \frac{b}{x+a} + \frac{b}{a-x},$$

to represent a pair of soft walls parallel to the y-z plane and located at $x = a$ and $x = -a$.

For convenience, we define:

$$L(\mathbf{q}', \mathbf{q}) \equiv \frac{1}{2}\left(\sum_{i=1}^{3} K_i[u_i(\mathbf{q}', \mathbf{q})]^2\right) + \lambda d_{33}(\mathbf{q})$$

2.2. Buckling constraints. We impose the following clamped-clamped constraints on the rod:

$$\mathbf{r}(0) = (0, 0, 0), \quad x(1) = y(1) = 0, \quad \mathbf{q}(0) = \mathbf{q}(1) = (0, 0, 0, 1). \tag{2.1}$$

The constraints on $\mathbf{r}$ require that the ends of the rod lie on the z-axis (with the $s = 0$ end at the origin). The constraints on $\mathbf{q}$ require that the directors at the ends of the rod be aligned with the standard axes, so that in particular the tangent vectors at the ends are vertical. Fig. 2.1 illustrates two sample 3D configurations consistent with these constraints.

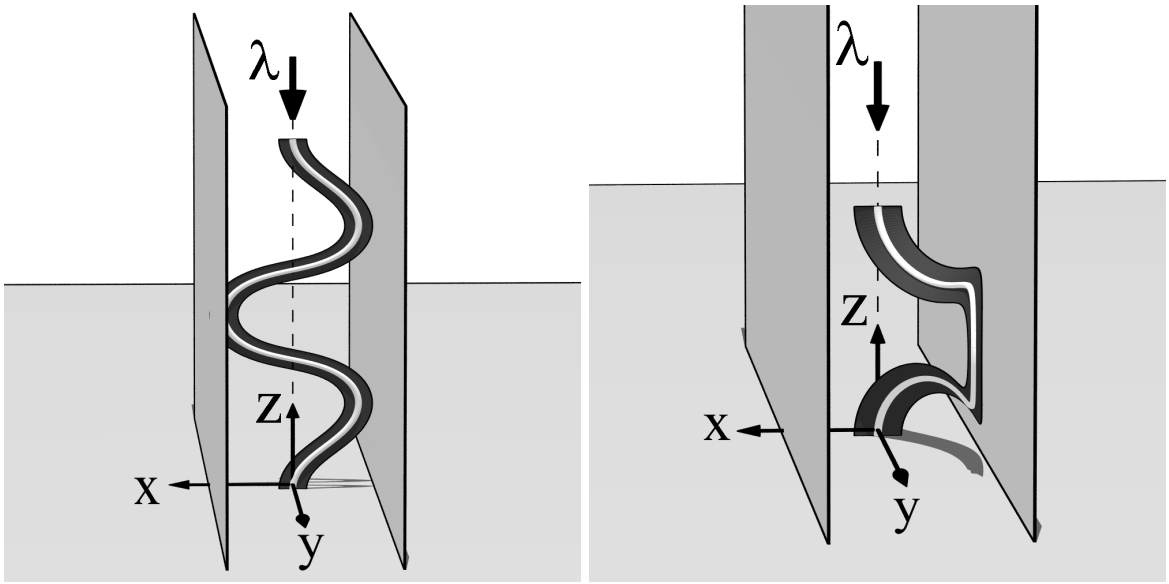

FIG. 2.1. *Two equilibrium configurations for an elastic rod buckling into a pair of "soft" walls. The centerline* $\mathbf{r}$ *of the rod is drawn as a tube, and the director* $\mathbf{d}_1$ *as a ribbon. A load* λ *is applied, and the ends are held vertical, untwisted, and along the z-axis.*

We note that since we begin our computations with a straight untwisted rod and never introduce relative twist between the ends, our computations will miss many highly twisted solutions consistent with (2.1), e.g., those one would find by starting with a straight rod with an integer number of full twists before buckling begins. We note also that with these constraints, lateral forces in the x and y directions may be present, and that while the z-force is known to equal λ, these lateral forces are unknowns of the problem (and, indeed, the x component depends on s due to the wall potential).

The stiffnesses K_1 and K_2 are proportional to the moments of inertia of the elliptical cross-section about $\mathbf{d}_1$ and $\mathbf{d}_2$ respectively, and the boundary conditions on $\mathbf{q}$ mandate that in the unbuckled configuration of the rod, $\mathbf{d}_1$ is perpendicular to the walls. Hence, when $K_2 < K_1$, the unbuckled rod has its major axis parallel to the wall; when $K_2 > K_1$, its major axis is perpendicular to the wall; and when $K_2 = K_1$, the cross-section is circular.

2.3. The variational problem useful for computation. It will be helpful to view this variational problem in two slightly different ways. First, we can consider E to be a functional of both $\mathbf{r}$ and $\mathbf{q}$. Equilibria of the rod are then critical points of this functional $E[\mathbf{r}, \mathbf{q}]$ subject to the pointwise constraint $\mathbf{r}'(s) = \mathbf{d}_3(\mathbf{q}(s))$ and the boundary conditions (2.1). These equilibria can be found by solving the standard Euler-Lagrange equations, which can be written in the following first-order Hamiltonian form [3], with $\mathbf{n} \in \mathbb{R}^3$ the variable conjugate to $\mathbf{r}$ (and representing the force in the rod), and $\boldsymbol{\mu} \in \mathbb{R}^4$ the variable conjugate to $\mathbf{q}$:

$$\begin{aligned}
\mathbf{r}' &= \mathbf{d}_3(\mathbf{q}), \\
\mathbf{q}' &= \frac{1}{4}\sum_{i=1}^{3} \frac{\boldsymbol{\mu}^T \mathbf{B}_i \mathbf{q}}{K_i} \mathbf{B}_i \mathbf{q}, \\
\mathbf{n}' &= V_{\mathbf{r}}(\mathbf{r}), \\
\boldsymbol{\mu}' &= \frac{1}{4}\sum_{i=1}^{3} \frac{\boldsymbol{\mu}^T \mathbf{B}_i \mathbf{q}}{K_i} \mathbf{B}_i \boldsymbol{\mu} - [(\mathbf{d}_3)_{\mathbf{q}}(\mathbf{q})]^T \mathbf{n}.
\end{aligned}$$

Here and throughout, subscripting by $\mathbf{r}$ or $\mathbf{q}$ denotes partial differentiation, e.g., the term $(\mathbf{d}_3)_{\mathbf{q}}$ represents the 3×4 matrix $\frac{\partial \mathbf{d}_3}{\partial \mathbf{q}}$. We solve this system of first-order ODEs subject to the 13 boundary conditions from Eq. (2.1) plus the boundary condition $n_3(1) = -\lambda$ representing the imposed load. Solutions of this boundary value problem (BVP) were obtained using AUTO, beginning with the unbuckled configuration $\mathbf{r}(s) = (0, 0, s), \mathbf{q}(s) = (0, 0, 0, 1)$, which is an equilibrium for any value of λ. Parameter continuation in λ was then performed to track families of equilibria, including the detection of bifurcating branches.[1]

2.4. The variational problem useful for stability theory. A second perspective, which we will use for determining stability, is to view E as a functional of $\mathbf{q}$ alone. This perspective is possible because $\mathbf{r}$ is completely determined from $\mathbf{q}$ via the constraint $\mathbf{r}' = \mathbf{d}_3(\mathbf{q})$ combined with the initial condition $\mathbf{r}(0) = \mathbf{0}$:

$$\mathbf{r}(s) = \int_0^s \mathbf{d}_3(\mathbf{q}(\sigma)) d\sigma.$$

[1] In the numerical computations, the boundary condition $q_4(0) = 1$ was replaced by the condition $\mu_4(0) = 0$. This change removes a gauge symmetry of the problem that results from the representation of elements $(\mathbf{d}_1, \mathbf{d}_2, \mathbf{d}_3)$ of the 3-dimensional group $SO(3)$ by $\mathbf{q} \in \mathbb{R}^4$. Without this change, there would be an entire line of solutions to the BVP at each value of λ, which is undesirable for numerical computations. The condition $q_4(0) = 1$ can safely be dropped, since the quantity $|\mathbf{q}|$ is conserved by the differential equations, so the remaining boundary conditions on $\mathbf{q}$ will guarantee that $q_4(0) = 1$ without it being explicitly enforced in the computations.

In this view, we rewrite the boundary conditions $x(1) = y(1) = 0$ as isoperimetric constraints:

$$\int_0^1 d_{31}(\mathbf{q}(s))ds = \int_0^1 d_{32}(\mathbf{q}(s))ds = 0.$$

Thus, we seek critical points of the functional

$$E[\mathbf{q}] = \int_0^1 \left[L(\mathbf{q}'(s), \mathbf{q}(s)) + V\left(\int_0^s \mathbf{d}_3(\mathbf{q}(\sigma))d\sigma \right) \right] \, ds$$

subject to

$$\mathbf{q}(0) = \mathbf{q}(1) = (0, 0, 0, 1), \quad \int_0^1 d_{31}(\mathbf{q}(s)) \, ds = \int_0^1 d_{32}(\mathbf{q}(s)) \, ds = 0.$$

2.5. The 2D case. In the 2D case, the rod can be described by a single unknown, the angle $\theta(s)$ that the rod's tangent vector makes with the upward axis at arclength position s. For consistency with the 3D coordinates, we denote the centerline $\mathbf{r}(s)$ by $(x(s), z(s))$, and the inextensibility-unshearability constraint simply takes the form $(x', z') = (\sin\theta, \cos\theta)$. In place of the three strains, we have the quantity $\theta'(s)$, which represents the rate of bending at position s.

The energy takes the form

$$E \equiv \int_0^1 \left[\frac{\theta'(s)^2}{2} + \lambda \cos\theta(s) + V(x(s)) \right] \, ds$$

(a stiffness parameter K_1 that multiplies the bending energy term $\frac{\theta'(s)^2}{2}$ was removed by choice of units). We consider two sets of boundary conditions, the clamped-clamped case

$$x(0) = x(1) = z(0) = 0, \ \theta(0) = \theta(1) = 0, \tag{2.2}$$

and the pinned-pinned case

$$x(0) = x(1) = z(0) = 0, \ \theta'(0) = \theta'(1) = 0. \tag{2.3}$$

The equations used to determine equilibria are:

$$\begin{aligned} x' &= \sin\theta \\ z' &= \cos\theta \\ \theta' &= w \\ w' &= -\lambda \sin\theta - n_x \cos\theta \\ n_x' &= V_x(x) \end{aligned}$$

subject to either the 5 boundary conditions in (2.2) or in (2.3).

For the variational problem relevant for stability, we consider the energy as a functional of θ only, which takes the form:

$$E \equiv \int_0^1 \left[\frac{\theta'(s)^2}{2} + \lambda \cos\theta(s) + V\left(\int_0^s \sin\theta(\sigma) d\sigma \right) \right] \, ds,$$

subject to either the clamped-clamped conditions

$$\theta(0) = \theta(1) = 0, \quad \int_0^1 \sin\theta(s) ds = 0.$$

or the pinned-pinned conditions

$$\theta'(0) = \theta'(1) = 0, \quad \int_0^1 \sin\theta(s) ds = 0.$$

3. Computing the index for the soft wall. We now turn to the stability theory that is the focus of this article. As before, we begin with a detailed presentation of the full 3D problem, and turn at the end to a summary of the simpler 2D analogue.

Assume that we have found an equilibrium $\mathbf{q}_0$ of $E[\mathbf{q}]$. To determine its stability, we consider *allowed variations* $\delta\mathbf{q}$ of $\mathbf{q}$, i.e., functions $\delta\mathbf{q}$ for which $\mathbf{q}_0 + \epsilon\delta\mathbf{q}$ obeys the boundary conditions and constraints on $\mathbf{q}$ to first order in ϵ:

$$\delta\mathbf{q}(0) = \delta\mathbf{q}(1) = (0,0,0,0), \quad \int_0^1 \delta\mathbf{q}(s)^T (d_{31})^0_{\mathbf{q}}(s) \, ds = \int_0^1 \delta\mathbf{q}(s)^T (d_{32})^0_{\mathbf{q}}(s) \, ds = 0, \tag{3.1}$$

where a superscript 0 denotes evaluation at the equilibrium $\mathbf{q}_0$.

We define the index to be the dimension of a maximal (deleted) subspace of allowed variations $\delta\mathbf{q}$ on which $E[\mathbf{q}_0 + \epsilon\delta\mathbf{q}] < E[\mathbf{q}_0]$ for $\epsilon > 0$ sufficiently small. If the index is zero (i.e., for all allowed variations $\delta\mathbf{q}$, $E[\mathbf{q}_0 + \epsilon\delta\mathbf{q}] \geq E[\mathbf{q}_0]$ for ϵ sufficiently small), then we will say that $\mathbf{q}_0$ is a *stable* equilibrium.

We note first a property of the functional E peculiar to the example at hand, namely that it is invariant to a scaling of $\mathbf{q}$, i.e., for any function $\alpha(s)$,

$$E[\alpha\mathbf{q}] = E[\mathbf{q}].$$

This degeneracy arises from our use of $\mathbf{q} \in \mathbb{R}^4$ to represent the three-dimensional space $SO(3)$ of directors. If we write $\delta\mathbf{q}(s)$ as $\beta(s)\mathbf{q}_0(s) + \mathbf{v}(s)$, where at each s, $\mathbf{v}(s) \perp \mathbf{q}_0(s)$, then

$$E[\mathbf{q}_0 + \epsilon\delta\mathbf{q}] = E[(1+\epsilon\beta)\mathbf{q}_0 + \epsilon\mathbf{v}] = E[\mathbf{q}_0 + \frac{\epsilon}{1+\epsilon\beta}\mathbf{v}]$$

Therefore, we can say that $E[\mathbf{q}_0 + \epsilon\delta\mathbf{q}] < E[\mathbf{q}_0]$ for ϵ sufficiently small if and only if $E[\mathbf{q}_0 + \epsilon\mathbf{v}] < E[\mathbf{q}_0]$ for ϵ sufficiently small. Thus, it is sufficient to consider only those allowed variations $\delta\mathbf{q}$ that are orthogonal to $\mathbf{q}_0$ at each s. Since $\{\mathbf{B}_1\mathbf{q}_0(s), \mathbf{B}_2\mathbf{q}_0(s), \mathbf{B}_3\mathbf{q}_0(s)\}$ is a basis for the orthogonal complement of $\mathbf{q}_0(s)$ in $\mathbb{R}^4$, we define at each s a projection:

$$\mathbf{\Pi}(s) = \begin{bmatrix} \mathbf{B}_1\mathbf{q}_0(s) & \mathbf{B}_2\mathbf{q}_0(s) & \mathbf{B}_3\mathbf{q}_0(s) \end{bmatrix} \in \mathbb{R}^{4\times 3}$$

and let

$$\delta\mathbf{q}(s) = \mathbf{\Pi}(s)\boldsymbol{\zeta}(s)$$

for some $\boldsymbol{\zeta}(s) \in \mathbb{R}^3$. Since projected constraints will appear throughout Sec. 3, we define:

$$\mathbf{M}(s) \equiv \mathbf{\Pi}(s)^T[(\mathbf{d}_3)^0_{\mathbf{q}}(s)]^T \in \mathbb{R}^{3\times 3},$$

and for $j = 1, 2, 3$, we let

$$\mathbf{T}_j(s) = \mathbf{\Pi}(s)^T(d_{3j})^0_{\mathbf{q}}(s),$$

the jth column of $\mathbf{M}$. By direct computation, we may show that the 3rd row of $\mathbf{M}$ vanishes.

Because of the conditions (3.1) imposed on $\delta\mathbf{q}$, we have the following conditions imposed on $\boldsymbol{\zeta}$:

$$\boldsymbol{\zeta}(0) = \boldsymbol{\zeta}(1) = (0,0,0), \quad \int_0^1 \boldsymbol{\zeta}(s)^T\mathbf{T}_1(s)\,ds = \int_0^1 \boldsymbol{\zeta}(s)^T\mathbf{T}_2(s)\,ds = 0. \tag{3.2}$$

3.1. The second variation. Next we consider the second variation of E, which is obtained by substituting $\mathbf{q} = \mathbf{q}_0 + \epsilon\delta\mathbf{q}$ into $E[\mathbf{q}]$ and computing the ϵ^2 term in the Taylor expansion:

$$\begin{aligned}\delta^2 E[\delta\mathbf{q}] = \int_0^1 \big[&\delta\mathbf{q}(s)^T L^0_{\mathbf{qq}}(s)\delta\mathbf{q}(s) + \delta\mathbf{q}'(s)^T L^0_{\mathbf{q}'\mathbf{q}}(s)\delta\mathbf{q}(s) + \delta\mathbf{q}(s)^T L^0_{\mathbf{qq}'}(s)\delta\mathbf{q}'(s)\\ &+\delta\mathbf{q}'(s)^T L^0_{\mathbf{q}'\mathbf{q}'}(s)\delta\mathbf{q}'(s) + \delta\mathbf{r}(s)^T V^0_{\mathbf{rr}}(s)\delta\mathbf{r}(s)\big]\,ds,\end{aligned} \tag{3.3}$$

where $\delta\mathbf{r}(s) = \int_0^s (\mathbf{d}_3)^0_{\mathbf{q}}(\sigma)\delta\mathbf{q}(\sigma)d\sigma$. Inserting $\delta\mathbf{q} = \mathbf{\Pi}\boldsymbol{\zeta}$ into Eq. (3.3), and integrating by parts terms starting with $\boldsymbol{\zeta}'(s)^T$, we find:

$$\delta^2 E[\mathbf{\Pi}\boldsymbol{\zeta}] = \int_0^1 \left[\boldsymbol{\zeta}(s)^T(\mathcal{S}\boldsymbol{\zeta})(s) + \delta\mathbf{r}(s)^T V^0_{\mathbf{rr}}(s)\delta\mathbf{r}(s)\right] ds,$$

where $\mathcal{S}$ is the Sturm-Liouville operator

$$\mathcal{S}\boldsymbol{\zeta} = -\frac{d}{ds}\left(\mathbf{P}\boldsymbol{\zeta}' + \mathbf{C}^T\boldsymbol{\zeta}\right) + \mathbf{C}\boldsymbol{\zeta}' + \mathbf{Q}\boldsymbol{\zeta},$$

with coefficient matrices:

$$\begin{aligned}\mathbf{P} &= \mathbf{\Pi}^T L^0_{\mathbf{q}'\mathbf{q}'}\mathbf{\Pi},\\ \mathbf{C} &= (\mathbf{\Pi}')^T L^0_{\mathbf{q}'\mathbf{q}'}\mathbf{\Pi} + \mathbf{\Pi}^T L^0_{\mathbf{qq}'}\mathbf{\Pi},\\ \mathbf{Q} &= (\mathbf{\Pi}')^T L^0_{\mathbf{q}'\mathbf{q}'}\mathbf{\Pi}' + \mathbf{\Pi}^T L^0_{\mathbf{qq}}\mathbf{\Pi} + \mathbf{\Pi}^T L^0_{\mathbf{qq}'}\mathbf{\Pi}' + (\mathbf{\Pi}')^T L^0_{\mathbf{q}'\mathbf{q}}\mathbf{\Pi}.\end{aligned}$$

Note that the integral operator that defines $\delta\mathbf{r}$:

$$\delta\mathbf{r}(s) = \int_0^s (\mathbf{d}_3)^0_{\mathbf{q}}(\sigma)\mathbf{\Pi}(\sigma)\boldsymbol{\zeta}(\sigma)d\sigma = \int_0^s \mathbf{M}(\sigma)^T\boldsymbol{\zeta}(\sigma)d\sigma$$

is a linear functional of $\boldsymbol{\zeta}$, which we denote by $\mathcal{K} : L^2(0,1) \to L^2(0,1)$:

$$(\mathcal{K}\mathbf{f})(s) \equiv \int_0^s \mathbf{M}(\sigma)^T\mathbf{f}(\sigma)d\sigma.$$

Thus, the second variation can be rewritten as:

$$\delta^2 E = \int_0^1 \left[\boldsymbol{\zeta}(s)^T(\mathcal{S}\boldsymbol{\zeta})(s) + \boldsymbol{\zeta}(s)^T(\mathcal{K}^T V^0_{\mathbf{rr}}\mathcal{K}\boldsymbol{\zeta})(s)\right] ds.$$

3.2. An alternate form of the second variation. The adjoint operator $\mathcal{K}^T$ has an inconvenient form that does not readily yield a computational implementation via an IVP, so we now transform to a slightly different second variation. First we note that since the function $V(\mathbf{r})$ depends only on x, the only non-zero entry in $V^0_{\mathbf{rr}}$ is the upper-left entry V^0_{xx}. We define a new linear operator by:

$$(\mathcal{L}\mathbf{f})(s) \equiv -\int_s^1 \mathbf{M}(\sigma)^T\mathbf{f}(\sigma)d\sigma,$$

and observe that, for those $\boldsymbol{\zeta}$ that satisfy (3.2),

$$\mathcal{K}\boldsymbol{\zeta} - \mathcal{L}\boldsymbol{\zeta} = \int_0^1 \mathbf{M}(\sigma)^T\boldsymbol{\zeta}(\sigma)d\sigma = \begin{bmatrix} \int_0^1 \boldsymbol{\zeta}(\sigma)^T\mathbf{T}_1(\sigma)\,d\sigma \\ \int_0^1 \boldsymbol{\zeta}(\sigma)^T\mathbf{T}_2(\sigma)\,d\sigma \\ \int_0^1 \boldsymbol{\zeta}(\sigma)^T\mathbf{T}_3(\sigma)\,d\sigma \end{bmatrix} = \begin{bmatrix} 0 \\ 0 \\ \int_0^1 \boldsymbol{\zeta}(\sigma)^T\mathbf{T}_3(\sigma)\,d\sigma \end{bmatrix}.$$

Therefore, since the third column of $V^0_{\mathbf{rr}}$ is zero,

$$V^0_{\mathbf{rr}}\mathcal{K}\boldsymbol{\zeta} - V^0_{\mathbf{rr}}\mathcal{L}\boldsymbol{\zeta} = \mathbf{0}.$$

Then,

$$\boldsymbol{\zeta}^T\mathcal{K}^TV^0_{\mathbf{rr}}\mathcal{K}\boldsymbol{\zeta} = (\mathcal{K}\boldsymbol{\zeta})^T\,V^0_{\mathbf{rr}}\mathcal{K}\boldsymbol{\zeta} = (\mathcal{K}\boldsymbol{\zeta})^T\,V^0_{\mathbf{rr}}\mathcal{L}\boldsymbol{\zeta} = \left(\mathcal{L}\boldsymbol{\zeta} + \int_0^1 \mathbf{M}(\sigma)^T\boldsymbol{\zeta}(\sigma)\,d\sigma\right)^T V^0_{\mathbf{rr}}\mathcal{L}\boldsymbol{\zeta}.$$

Finally, note that

$$\left(\int_0^1 \mathbf{M}(\sigma)^T\boldsymbol{\zeta}(\sigma)\,d\sigma\right)^T V^0_{\mathbf{rr}}\mathcal{L}\boldsymbol{\zeta} = \begin{bmatrix}0 & 0 & \int_0^1 \boldsymbol{\zeta}(\sigma)^T\mathbf{T}_3(\sigma)\,d\sigma\end{bmatrix} \begin{bmatrix} V^0_{xx} & 0 & 0 \\ 0 & 0 & 0 \\ 0 & 0 & 0 \end{bmatrix} \mathcal{L}\boldsymbol{\zeta} = 0.$$

So,

$$\boldsymbol{\zeta}^T\mathcal{K}^TV^0_{\mathbf{rr}}\mathcal{K}\boldsymbol{\zeta} = (\mathcal{L}\boldsymbol{\zeta})^T\,V^0_{\mathbf{rr}}\mathcal{L}\boldsymbol{\zeta} = \boldsymbol{\zeta}^T\mathcal{L}^TV^0_{\mathbf{rr}}\mathcal{L}\boldsymbol{\zeta},$$

which means that we may rewrite the second variation as:

$$\delta^2E = \int_0^1 \left[\boldsymbol{\zeta}(s)^T(\mathcal{S}\boldsymbol{\zeta})(s) + \boldsymbol{\zeta}(s)^T(\mathcal{L}^TV^0_{\mathbf{rr}}\mathcal{L}\boldsymbol{\zeta})(s)\right]ds = \int_0^1 \boldsymbol{\zeta}(s)^T[(\mathcal{S} + \mathcal{L}^TV^0_{\mathbf{rr}}\mathcal{L})\boldsymbol{\zeta}](s)\,ds.$$

Thus, we have a problem in the form of a classic isoperimetrically constrained calculus of variations problem, but with the integrodifferential second variation operator

$$\mathcal{O} \equiv \mathcal{S} + \mathcal{L}^TV^0_{\mathbf{rr}}\mathcal{L}.$$

The theory presented in [14] is an operator-based derivation of the stability index for isoperimetrically constrained calculus of variations problems, and we now show that this theory may readily be extended to $\mathcal{O}$.

3.3. Properties of the operator $\mathcal{O}$. We begin by defining some notation. For any $\sigma \leq 1$, we let $\mathcal{H}(\sigma)$ denote the Sobolev space of $\mathbb{R}^3$-functions with square-integrable weak second derivatives on the interval $(0, \sigma)$, and

$$\mathcal{H}_d(\sigma) \equiv \{\boldsymbol{\zeta} \in \mathcal{H}(\sigma) : \boldsymbol{\zeta}(0) = \boldsymbol{\zeta}(\sigma) = \mathbf{0}\}.$$

Let $L^2(0, \sigma)$ denote the space of all square-integrable $\mathbb{R}^3$-functions on $(0, \sigma)$. The operator $\mathcal{L}$ has a natural restriction to $L^2(0, \sigma)$, namely:

$$(\mathcal{L}\mathbf{f})(s) = -\int_s^\sigma \mathbf{M}(\tau)^T \mathbf{f}(\tau) d\tau.$$

First, we determine $\mathcal{L}^T$ on $L^2(0, \sigma)$. For arbitrary functions $\mathbf{f}, \mathbf{g} \in L^2(0, \sigma)$, we compute:

$$\begin{aligned}
\int_0^\sigma \mathbf{g}(s)^T (\mathcal{L}\mathbf{f})(s)\, ds &= -\int_0^\sigma \mathbf{g}(s)^T \left[\int_s^\sigma \mathbf{M}(\tau)^T \mathbf{f}(\tau) d\tau\right] ds = -\int_0^\sigma \int_s^\sigma \mathbf{g}(s)^T \mathbf{M}(\tau)^T \mathbf{f}(\tau) d\tau ds \\
&= -\int_0^\sigma \int_0^\tau \mathbf{g}(s)^T \mathbf{M}(\tau)^T \mathbf{f}(\tau) ds d\tau = -\int_0^\sigma \int_0^\tau \mathbf{f}(\tau)^T \mathbf{M}(\tau) \mathbf{g}(s) ds d\tau \\
&= \int_0^\sigma \mathbf{f}(\tau)^T \left(-\mathbf{M}(\tau) \int_0^\tau \mathbf{g}(s) ds\right) d\tau
\end{aligned}$$

So, the adjoint operator is

$$(\mathcal{L}^T \mathbf{g})(\tau) = -\mathbf{M}(\tau) \int_0^\tau \mathbf{g}(s) ds,$$

and it has domain of definition $L^2(0, \sigma)$.

LEMMA 3.1. *The operator $\mathcal{O} : \mathcal{H}_d(\sigma) \subset L^2(0, \sigma) \to L^2(0, \sigma)$ is self-adjoint.*

Proof: As is well-known, the Sturm-Liouville operator $\mathcal{S}$ is self-adjoint on $\mathcal{H}_d(\sigma)$. Furthermore, since multiplication by $V_{\mathbf{rr}}^0$ is a self-adjoint operator on $L^2(0, \sigma)$, we can see that $\mathcal{L}^T V_{\mathbf{rr}}^0 \mathcal{L}$ is also a self-adjoint operator on $L^2(0, \sigma)$, which implies that $\mathcal{O}$ is self-adjoint on $\mathcal{H}_d(\sigma)$. □

LEMMA 3.2. *The spectrum of $\mathcal{O}$ on $\mathcal{H}_d(\sigma)$ consists of isolated eigenvalues $\rho_1(\sigma) \leq \rho_2(\sigma) \leq \ldots$ each with finite (geometric) multiplicity.*

Proof (follows closely the proof of Property 1 in [14]): Equivalently, we show that $\mathcal{O}$ has no essential spectrum.[2] Assume ρ is in the essential spectrum of $\mathcal{O}$. Then by definition ([2], p. 206), there exists a sequence $\boldsymbol{\zeta}_j \in \mathcal{H}_d(\sigma)$ with

(a) $\inf_j \|\boldsymbol{\zeta}_j\| > 0$,

(b) $\lim_{j\to\infty} \int_0^\sigma \boldsymbol{\zeta}_j(s)^T \mathbf{h}(s)\, ds = 0, \forall \mathbf{h} \in L^2(0, \sigma)$ (weak convergence of $\boldsymbol{\zeta}_j$ to $\mathbf{0}$),

(c) $(\mathcal{O} - \rho\mathcal{I})\boldsymbol{\zeta}_j \to \mathbf{0}$ (strong convergence to $\mathbf{0}$ in $L^2(0, \sigma)$).

The operator $\mathcal{L}$ is compact [16, p. 385], and, therefore, so is $\mathcal{L}^T$ [10, p. 159]. Thus, $\mathcal{L}^T V_{\mathbf{rr}}^0 \mathcal{L}$ is a compact operator [10, p. 158], and therefore transforms the weakly convergent sequence $\boldsymbol{\zeta}_j$ into a strongly convergent sequence ([2], p. 39), i.e., $\mathcal{L}^T V_{\mathbf{rr}}^0 \mathcal{L}\boldsymbol{\zeta}_j \to \mathbf{0}$. Applying this to (c), we see that

[2] There is some variation in how the essential spectrum is defined. Here we take the definition set forth in [2].

$(\mathcal{S}-\rho\mathcal{I})\boldsymbol{\zeta}_j \to \mathbf{0}$, which, combined with (a) and (b), shows that $\mathcal{S}$ has ρ as part of its essential spectrum. However, under the assumption that $\mathbf{P}$ is positive definite (which is true for our choice of L), a Sturm-Liouville operator $\mathcal{S}$ has no essential spectrum (see, for example, [17]). Thus we arrive at a contradiction and conclude that the essential spectrum of $\mathcal{O}$ is empty. □

We denote the $L^2(0,\sigma)$-orthonormal eigenfunctions of $\mathcal{O}$ by $\boldsymbol{\zeta}_j(s;\sigma) \in \mathcal{H}_d(\sigma)$, i.e.,

$$\mathcal{O}\boldsymbol{\zeta}_j(s;\sigma) = \rho_j(\sigma)\boldsymbol{\zeta}_j(s;\sigma),\ 0 < s < \sigma.$$

Next, for $m \geq 1$, define the following spaces:

$$\mathcal{B}_m(\sigma) \equiv \left\{ \boldsymbol{\zeta} \in \mathcal{H}_d(\sigma) : \int_0^\sigma \boldsymbol{\zeta}(s)^T\boldsymbol{\zeta}(s)\,ds = 1,\ \int_0^\sigma \boldsymbol{\zeta}(s)^T\boldsymbol{\zeta}_1(s;\sigma)\,ds = \cdots = \int_0^\sigma \boldsymbol{\zeta}(s)^T\boldsymbol{\zeta}_{m-1}(s;\sigma)\,ds = 0 \right\}.$$

LEMMA 3.3. *Each eigenvalue $\rho_j(\sigma)$ is a monotonically decreasing function of σ.*

Proof (follows closely the proof of Property 2 in [14]): The operator $\mathcal{O}$ is self-adjoint, bounded below, and satisfies Lemma 3.2. Further, $\mathcal{H}_d(\sigma)$ is dense in $L^2(0,\sigma)$. Therefore, the eigenvalues $\rho_j(\sigma)$ are given by a variational principle [21, p. 6]:

$$\rho_m(\sigma) = \min_{\boldsymbol{\zeta}\in\mathcal{B}_m(\sigma)} \int_0^\sigma \boldsymbol{\zeta}(s)^T(\mathcal{O}\boldsymbol{\zeta})(s)\,ds. \tag{3.4}$$

Consider $\sigma_1 < \sigma_2$. Let the functions $\boldsymbol{\psi}_i(s),\ \ i = 1,\ldots,m$ be defined on $0 \leq s \leq \sigma_2$ by:

$$\boldsymbol{\psi}_i(s) \equiv \begin{cases} \boldsymbol{\zeta}_i(s;\sigma_1) & 0 \leq s \leq \sigma_1, \\ \mathbf{0} & \sigma_1 < s \leq \sigma_2. \end{cases}$$

Now determine a_k so that $\sum_{k=1}^m (a_k)^2 = 1$ and such that $\boldsymbol{\zeta} = \sum_{k=1}^m a_k\boldsymbol{\psi}_k(s)$ is orthogonal to every element of $\mathrm{span}(\boldsymbol{\zeta}_1(s;\sigma_2),\cdots,\boldsymbol{\zeta}_{m-1}(s;\sigma_2))$, and hence an element of $\mathcal{B}_m(\sigma_2)$; since we have $m-1$ orthogonality conditions to satisfy and m coefficients a_k at our disposal, this can always be done by solving an $(m-1)$-by-m linear system and rescaling. Inserting $\boldsymbol{\zeta}(s)$ into (3.4), we have:

$$\begin{aligned} \rho_m(\sigma_2) &\leq \int_0^{\sigma_2} \left[\sum_{i=1}^m a_i\boldsymbol{\psi}_i(s)\right]^T \mathcal{O}\left[\sum_{k=1}^m a_k\boldsymbol{\psi}_k(s)\right] ds \\ &= \int_0^{\sigma_1} \left[\sum_{i=1}^m a_i\boldsymbol{\zeta}_i(s;\sigma_1)\right]^T \mathcal{O}\left[\sum_{k=1}^m a_k\boldsymbol{\zeta}_k(s;\sigma_1)\right] ds. \end{aligned}$$

Finally, we exploit the fact that $\{\boldsymbol{\zeta}_i(s;\sigma_1)\}$ is a set of orthonormal eigenfunctions of $\mathcal{O}$ to find:

$$\rho_m(\sigma_2) \leq \sum_{i,k=1}^m a_i a_k \rho_k(\sigma_1)\delta_{ik} = \sum_{i=1}^m a_i^2\rho_i(\sigma_1) \leq \rho_m(\sigma_1).$$

□

LEMMA 3.4. *For σ sufficiently close to 0, $\rho_j(\sigma) > 0$, $\forall j$.*

Proof (follows closely the proof of Property 3 in [14]): Standard unconstrained quadratic form theory for Sturm-Liouville operators (see, e.g., [19]) shows that for σ sufficiently small,

$$\int_0^\sigma \boldsymbol{\zeta}(s)^T(\mathcal{S}\boldsymbol{\zeta})(s)\,ds > 0, \;\; \forall \boldsymbol{\zeta} \in \mathcal{H}_d(\sigma).$$

Then, for σ sufficiently small, since $V_{\mathbf{rr}}^0$ is positive semidefinite,

$$\int_0^\sigma \boldsymbol{\zeta}(s)^T(\mathcal{O}\boldsymbol{\zeta})(s)\,ds = \int_0^\sigma \boldsymbol{\zeta}(s)^T(\mathcal{S}\boldsymbol{\zeta})(s)\,ds + \int_0^\sigma (\mathcal{L}\boldsymbol{\zeta})(s)^T V_{\mathbf{rr}}^0(\mathcal{L}\boldsymbol{\zeta})(s)ds > 0 \;\; \forall \boldsymbol{\zeta} \in \mathcal{H}_d(\sigma).$$

For any j, we know that ρ_j satisfies $\mathcal{O}\boldsymbol{\zeta}_j = \rho_j \boldsymbol{\zeta}_j$ for $\boldsymbol{\zeta}_j \in \mathcal{H}_d(\sigma)$. Premultiplying this expression by $\boldsymbol{\zeta}_j^T$ and integrating from 0 to σ, we see that for sufficiently small σ, $\rho_j(\sigma) > 0$. □

3.4. Handling the isoperimetric constraints. We have shown that

$$\delta^2 E = \int_0^1 \boldsymbol{\zeta}(s)^T(\mathcal{O}\boldsymbol{\zeta})(s)\,ds,$$

and that the space of allowed variations is $\mathcal{H}_d^{cons}(1) \equiv \mathcal{H}_d(1) \cap \mathcal{T}^\perp$ where:

$$\mathcal{T}^\perp \equiv \{\boldsymbol{\zeta} \in L^2(0,1) : \int_0^1 \boldsymbol{\zeta}(s)^T\mathbf{T}_1(s)\,ds = \int_0^1 \boldsymbol{\zeta}(s)^T\mathbf{T}_2(s)\,ds = 0\}.$$

Further, we have proven several facts about the spectrum of $\mathcal{O}$ in Lemmas 3.1–3.4.

A definition of conjugate points appropriate to this isoperimetrically constrained setting is given in [14]. Since the space of allowed variations $\mathcal{H}_d^{cons}(1)$ is not dense in the range space $L^2(0,1)$ of $\mathcal{O}$, we introduce a new operator $\mathcal{Q}\mathcal{O}\mathcal{Q}$, where $\mathcal{Q}$ is the (self-adjoint) orthogonal projection from $L^2(0,1)$ to its subspace $\mathcal{T}^\perp$. The range space of $\mathcal{Q}\mathcal{O}\mathcal{Q}$ is $\mathcal{T}^\perp$, and $\mathcal{H}_d^{cons}(1)$ *is* dense in $\mathcal{T}^\perp$. Then, in analogy with the notation of Sec. 3.3, we define the spaces:

$$\mathcal{T}^\perp(\sigma) \equiv \{\boldsymbol{\zeta} \in L^2(0,\sigma) : \int_0^\sigma \boldsymbol{\zeta}(s)^T\mathbf{T}_1(s)\,ds = \int_0^\sigma \boldsymbol{\zeta}(s)^T\mathbf{T}_2(s)\,ds = 0\}.$$

and

$$\mathcal{H}_d^{cons}(\sigma) \equiv \mathcal{H}_d(\sigma) \cap \mathcal{T}^\perp(\sigma).$$

In [14], it is then shown that $\mathcal{Q}\mathcal{O}\mathcal{Q} : \mathcal{H}_d^{cons}(\sigma) \subset \mathcal{T}^\perp(\sigma) \to \mathcal{T}^\perp(\sigma)$ satisfies the corresponding versions of Lemmas 3.1–3.4. These Lemmas then show that the index equals the number of solutions $\sigma < 1$ to:

$$(\mathcal{Q}\mathcal{O}\mathcal{Q}\boldsymbol{\zeta})(s) = \mathbf{0}, \;\; 0 < s < \sigma, \;\; \boldsymbol{\zeta} \in \mathcal{H}_d^{cons}(\sigma),$$

so that this equation is the appropriate definition of conjugate point for this setting. Written out explicitly without the projection operator, the definition of conjugate point is:

$$(\mathcal{O}\boldsymbol{\zeta})(s) = \breve{c}_1\mathbf{T}_1(s) + \breve{c}_2\mathbf{T}_2(s), \;\; 0 < s < \sigma, \;\; \boldsymbol{\zeta} \in \mathcal{H}_d^{cons}(\sigma) \tag{3.5}$$

for some constants $\breve{c}_1$, $\breve{c}_2$.

3.5. Computing conjugate points. We now show that the equation $\mathcal{O}\boldsymbol{\zeta} = \breve{c}_1\mathbf{T}_1 + \breve{c}_2\mathbf{T}_2$ may be written as a first-order system of ordinary differential equations. We observe first that:

$$V^0_{\mathbf{rr}}\mathcal{L}\boldsymbol{\zeta} = V^0_{\mathbf{rr}}\mathcal{K}\boldsymbol{\zeta} = \begin{bmatrix} V^0_{xx}\delta x \\ 0 \\ 0 \end{bmatrix},$$

and thus,

$$(\mathcal{L}^T V^0_{\mathbf{rr}}\mathcal{L}\boldsymbol{\zeta})(\sigma) = -\mathbf{M}(\sigma)\begin{bmatrix} \int_0^\sigma V^0_{xx}(s)\delta x(s)ds \\ 0 \\ 0 \end{bmatrix} = -\begin{bmatrix} M_{11}(\sigma)\int_0^\sigma V^0_{xx}(s)\delta x(s)ds \\ M_{21}(\sigma)\int_0^\sigma V^0_{xx}(s)\delta x(s)ds \\ 0 \end{bmatrix},$$

since $M_{31} = 0$. So, $\mathcal{O}\boldsymbol{\zeta} = \breve{c}_1\mathbf{T}_1 + \breve{c}_2\mathbf{T}_2$ may be rewritten as:

$$\begin{aligned} -\frac{d}{d\sigma}\left(\mathbf{P}(\sigma)\boldsymbol{\zeta}'(\sigma) + \mathbf{C}(\sigma)^T\boldsymbol{\zeta}(\sigma)\right) + \mathbf{C}(\sigma)\boldsymbol{\zeta}'(\sigma) + \mathbf{Q}(\sigma)\boldsymbol{\zeta}(\sigma) \\ - \begin{bmatrix} M_{11}(\sigma)\int_0^\sigma V^0_{xx}(s)\delta x(s)ds \\ M_{21}(\sigma)\int_0^\sigma V^0_{xx}(s)\delta x(s)ds \\ 0 \end{bmatrix} = \breve{c}_1\mathbf{T}_1(\sigma) + \breve{c}_2\mathbf{T}_2(\sigma), \end{aligned}$$

or, defining $\boldsymbol{\eta} = \mathbf{P}\boldsymbol{\zeta}' + \mathbf{C}^T\boldsymbol{\zeta}$ and $Y(\sigma) = -\int_0^\sigma V^0_{xx}(s)\delta x(s)ds$, as the first-order system:

$$\begin{aligned} \boldsymbol{\zeta}' &= -\mathbf{P}^{-1}\mathbf{C}^T\boldsymbol{\zeta} + \mathbf{P}^{-1}\boldsymbol{\eta} \\ \boldsymbol{\eta}' &= \left(\mathbf{Q} - \mathbf{C}\mathbf{P}^{-1}\mathbf{C}^T\right)\boldsymbol{\zeta} + \mathbf{C}\mathbf{P}^{-1}\boldsymbol{\eta} - \breve{c}_1\mathbf{T}_1 - \breve{c}_2\mathbf{T}_2 + \begin{bmatrix} M_{11}Y \\ M_{21}Y \\ 0 \end{bmatrix}, \\ \delta x' &= M_{11}\zeta_1 + M_{21}\zeta_2, \\ Y' &= -V^0_{xx}\delta x. \end{aligned} \tag{3.6}$$

Thus, analogously to the presentation in [14], the general solution to $\mathcal{O}\boldsymbol{\zeta} = \breve{c}_1\mathbf{T}_1 + \breve{c}_2\mathbf{T}_2, \boldsymbol{\zeta}(0) = \mathbf{0}$ may be written as $c_1\boldsymbol{\zeta}_1 + c_2\boldsymbol{\zeta}_2 + c_3\boldsymbol{\zeta}_3 + \breve{c}_1\breve{\boldsymbol{\zeta}}_1 + \breve{c}_2\breve{\boldsymbol{\zeta}}_2$, where $\{\boldsymbol{\zeta}_1, \boldsymbol{\zeta}_2, \boldsymbol{\zeta}_3\}$ are a basis of solutions to $\mathcal{O}\boldsymbol{\zeta} = \mathbf{0}, \boldsymbol{\zeta}(0) = \mathbf{0}$ and for $j = 1, 2$, $\breve{\boldsymbol{\zeta}}_j$ is a solution to $\mathcal{O}\boldsymbol{\zeta} = \mathbf{T}_j, \boldsymbol{\zeta}(0) = \mathbf{0}$. Each of these functions may be computed as a solution to an IVP: for $\boldsymbol{\zeta}_j$, we solve Eq. (3.6) with $(\breve{c}_1, \breve{c}_2) = (0, 0)$ and the initial conditions

$$\boldsymbol{\zeta}(0) = \mathbf{0}, \quad \boldsymbol{\eta}(0) = \mathbf{e}_j, \quad \delta x(0) = 0, \quad Y(0) = 0,$$

while for $\breve{\boldsymbol{\zeta}}_j$, we solve Eq. (3.6) with $\breve{c}_k = \delta_{kj}$ and the initial conditions

$$\boldsymbol{\zeta}(0) = \mathbf{0}, \quad \boldsymbol{\eta}(0) = \mathbf{0}, \quad \delta x(0) = 0, \quad Y(0) = 0.$$

Conjugate points occur when at some $\sigma < 1$ a nontrivial member of this general solution vanishes and obeys the linearized integral constraints. This combination of conditions may be written in compact form as:

$$\det\begin{bmatrix} \mathbf{A}(\sigma) & \breve{\mathbf{A}}(\sigma) \\ \mathbf{F}(\sigma) & \breve{\mathbf{F}}(\sigma) \end{bmatrix} = 0,$$

where

$$\mathbf{A}(\sigma) = \begin{bmatrix}\boldsymbol{\zeta}_1(\sigma) & \boldsymbol{\zeta}_2(\sigma) & \boldsymbol{\zeta}_3(\sigma)\end{bmatrix} \in \mathbb{R}^{3\times 3}, \quad \breve{\mathbf{A}}(\sigma) = \begin{bmatrix}\breve{\boldsymbol{\zeta}}_1(\sigma) & \breve{\boldsymbol{\zeta}}_2(\sigma)\end{bmatrix} \in \mathbb{R}^{3\times 2},$$
$$\mathbf{F}(\sigma) \equiv \{f_{ij}(\sigma)\} = \begin{bmatrix}\int_0^\sigma \boldsymbol{\zeta}_1(\tau)^T\mathbf{T}_1(\tau)d\tau & \int_0^\sigma \boldsymbol{\zeta}_2(\tau)^T\mathbf{T}_1(\tau)d\tau & \int_0^\sigma \boldsymbol{\zeta}_3(\tau)^T\mathbf{T}_1(\tau)d\tau \\ \int_0^\sigma \boldsymbol{\zeta}_1(\tau)^T\mathbf{T}_2(\tau)d\tau & \int_0^\sigma \boldsymbol{\zeta}_2(\tau)^T\mathbf{T}_2(\tau)d\tau & \int_0^\sigma \boldsymbol{\zeta}_3(\tau)^T\mathbf{T}_2(\tau)d\tau\end{bmatrix} \in \mathbb{R}^{2\times 3},$$
$$\breve{\mathbf{F}}(\sigma) \equiv \{\breve{f}_{ij}(\sigma)\} = \begin{bmatrix}\int_0^\sigma \breve{\boldsymbol{\zeta}}_1(\tau)^T\mathbf{T}_1(\tau)d\tau & \int_0^\sigma \breve{\boldsymbol{\zeta}}_2(\tau)^T\mathbf{T}_1(\tau)d\tau \\ \int_0^\sigma \breve{\boldsymbol{\zeta}}_1(\tau)^T\mathbf{T}_2(\tau)d\tau & \int_0^\sigma \breve{\boldsymbol{\zeta}}_2(\tau)^T\mathbf{T}_2(\tau)d\tau\end{bmatrix} \in \mathbb{R}^{2\times 2}.$$

The integrals in $\mathbf{F}$ and $\breve{\mathbf{F}}$ may similarly be computed via an IVP, e.g.,

$$\frac{d}{d\sigma} f_{ij}(\sigma) = \boldsymbol{\zeta}_j(\sigma)^T\mathbf{T}_i(\sigma), \quad f_{ij}(0) = 0.$$

3.6. The 2D case. Recall that, for the 2D case, there is one unknown $\theta(s)$. The allowed variations ζ of θ obey either the linearized clamped-clamped conditions

$$\zeta(0) = \zeta(1) = 0, \ \int_0^1 \cos(\theta(s))\zeta(s)ds,$$

or the linearized pinned-pinned conditions

$$\zeta'(0) = \zeta'(1) = 0, \ \int_0^1 \cos(\theta(s))\zeta(s)ds.$$

The projection required with the Euler parameters $\mathbf{q}$ is no longer required.

The second variation again takes the form

$$\delta^2 E = \int_0^1 \left[\zeta(s)(\mathcal{S}\zeta)(s) + \zeta(s)(\mathcal{K}^T V_{xx}^0 \mathcal{K}\zeta)(s)\right] ds,$$

but now with $\mathcal{S}\zeta = -\zeta'' - \lambda\cos\theta\zeta$ and

$$(\mathcal{K}f)(s) = \int_0^s \cos\theta(\sigma) f(\sigma)d\sigma.$$

In the clamped-clamped case, the analysis of the second variation operator $\mathcal{O}$ proceeds exactly as in the 3D case, as does the incorporation of the isoperimetric constraints, leading to the conjugate point equation

$$\begin{aligned}\zeta' &= w \\ w' &= -\lambda\cos\theta\ \zeta + \cos\theta\ Y - c\cos\theta \\ \delta x' &= \cos\theta\ \zeta \\ Y' &= -V_{xx}^0 \delta x.\end{aligned}$$

and conjugate points determined by an analogous (but simpler) solution of initial value problem and determinant condition.

For the pinned-pinned case, a technical complication arises because the simple extension idea used to construct $\boldsymbol{\psi}$ introduces a discontinuity that makes $\boldsymbol{\psi}$ an illegal test function. Because of this, eigenvalues $\rho_m(\sigma)$ can potentially be increasing when they cross zero at a conjugate point, thus eliminating the simplistic notion that the number of conjugate points equals the number of negative eigenvalues. This technical computation is overcome by numerically determining $d\rho_m(\sigma)/d\sigma$ at each conjugate point, which allows an accounting of whether an eigenvalue is becoming negative or positive at each conjugate point. For an example of how this computation can be implemented, and a further discussion of this topic, see [13].

4. Verification of the index theory. We used AUTO to compute bifurcation diagrams of equilibrium rod configurations for the 3D problem, and we determined the stability index for each equilibrium by the procedure described in Sec. 3. The bifurcation diagrams plot the load λ on the vertical axis and the compression $1-z(1)$ on the horizontal axis. The line styles represent the index: solid black is stable (index 0), followed by solid gray (index 1), solid light gray (index 2), dashed black (index 3), dashed gray (index 4), and dashed light gray (index 5). One such bifurcation diagram is shown in Fig. 4.1. Before analyzing this diagram and how its structure depends on the

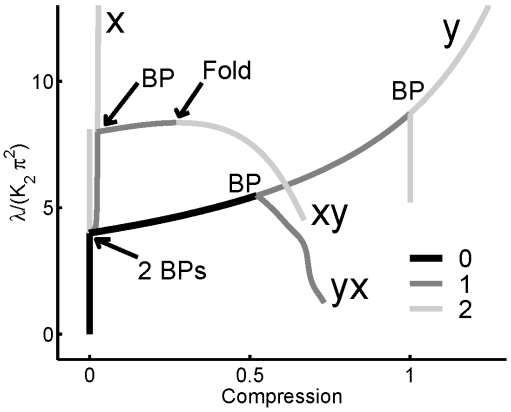

FIG. 4.1. *Portion of the bifurcation diagram for a rod with a circular cross-section ($K_1 = K_2 = 0.1, K_3 = 0.06$) buckling into soft walls with spacing parameter $a = 0.1$ and strength $b = 0.0001$. The label x corresponds to bending perpendicular to the wall, the label y to bending parallel to the wall. The label xy (respectively, yx) denotes a secondary bifurcating branch off of the x (respectively, y) branch containing configurations that are neither parallel nor perpendicular. Line styles represent the stability index: solid black for index 0 (stable), solid gray for index 1, and solid light gray for index 2. The index changes at folds and bifurcation points (BPs).*

rod and wall parameters, we first observe that the general properties of the index on this diagram serve to verify the theory from Sec. 3. Specifically, according to general bifurcation theory, changes in stability should generically occur exactly at bifurcation points and folds, and this is the case in Fig. 4.1. A fold occurs where a branch is horizontal, i.e., λ changes from increasing to decreasing, or vice versa. A bifurcation point is a point of intersection of two branches on the diagram. Due to the symmetry of the circular rod, all of the branches in Fig. 4.1 (except for the unbuckled branch) are double-covered, so all of the labeled bifurcation points are standard pitchfork bifurcations. Most

of the time, if we follow a branch as it bypasses a bifurcation point and continue to increase the compression, the rod will lose stability (cf. the two bifurcation points on branch y in Fig. 4.1), although in some instances we did observe a bifurcation point with the opposite behavior, including one case where a rod regained stability at a bifurcation point (see Fig. 5.10). Note that in Fig. 5.10, as in all our future bifurcation diagrams, we do not show all bifurcating branches, but their existence can be inferred from index changes that occur away from folds.

Note also that no stable branches are shown above a certain maximal value of λ. Our model does not include any self-contact forces for the rod itself, and for sufficiently high forces, the stable configurations involve rod self-contact. Our focus is on configurations at lower forces before self-contact is relevant, and in particular on the effect of the wall in stabilizing certain configurations. In the 2D problem (with the walls sufficiently close together), wall contact occurs before self-contact can take place, and we will see a wider range of λ values with stable solutions, since in the 2D setting, the rod can not bend or slide parallel to the walls to reach a self-contact configuration.

5. Results. We first present results for the 2D pinned-pinned rod, then for the 2D clamped-clamped rod, and finally for the 3D clamped-clamped rod (with the circular and elliptical cross-section cases presented separately).

5.1. 2D pinned-pinned rods. In Fig. 5.1, we show three bifurcation diagrams for the 2D pinned-pinned problem, two for a soft wall with $b = 10^{-4}$ and 10^{-5}, and one for a hard wall (the hard wall data was traced from [9] using the image-processing package SigmaScan). As $b \to 0$, the soft-wall

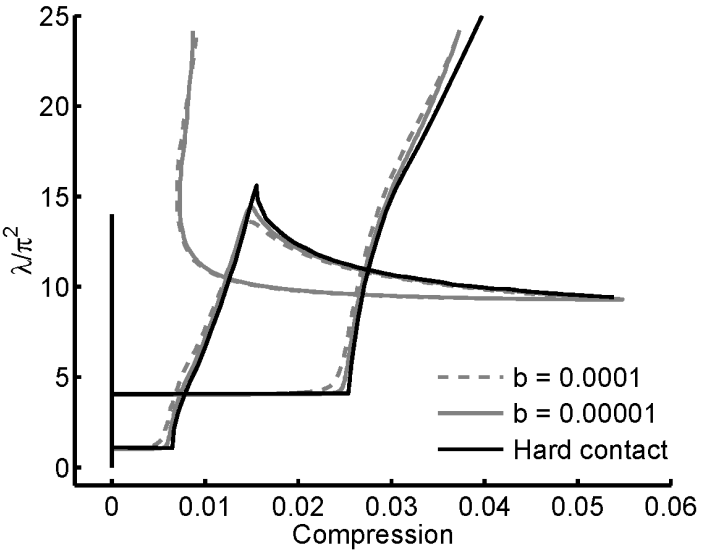

FIG. 5.1. *Convergence as $b \to 0$ of bifurcation diagrams for a 2D rod with pinned-pinned boundary conditions.*

diagrams appear to approach the hard-wall diagram (ignoring the extra branch in the soft-wall diagram not computed in the hard-wall case). Therefore, it seems plausible to use the stability

results for the soft wall case (with $b \approx 0$) to impute stability to the hard-wall case. For example, in Fig. 5.2, we show the soft wall diagram with $b = 10^{-5}$ with stability indicated by linestyle. For

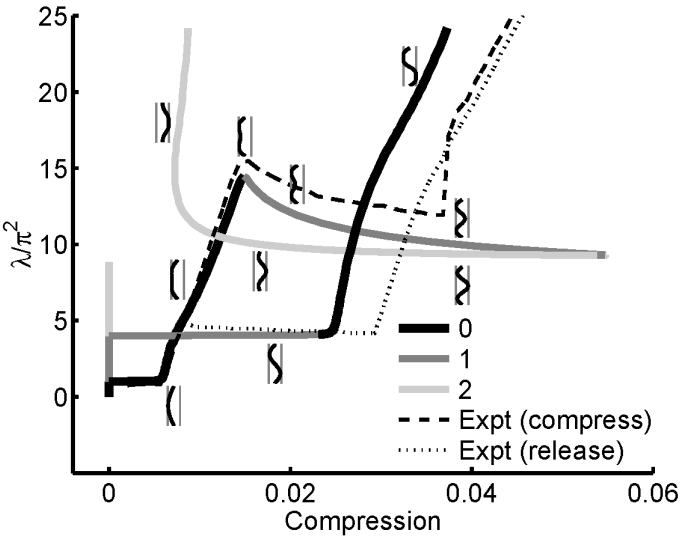

FIG. 5.2. *Bifurcation diagram for a 2D rod with pinned-pinned boundary conditions, with stability indicated by linestyle, and a few representative rod configurations sketched. Experimental results from [9] for a similar system are also shown.*

$\lambda < \pi^2$, the straight configuration (zero compression) is stable, as expected from standard rod theory. At $\lambda = \pi^2$, this configuration becomes unstable in favor of a branch of stable configurations bent toward either wall. As λ grows, the configuration becomes more mashed up against the wall (in the hard-wall limit, a line of contact emerges along this branch [9], but in the soft-wall case, this behavior is smoothed somewhat). At $\lambda \approx 15\pi^2$ (around the point where the portion of the rod near the wall begins to buckle away from the wall), this branch folds and becomes unstable. The second bifurcating branch off the zero-compression branch contains configurations with two turning points. These are initially unstable, but contact with the wall stabilizes them when the compression reaches approximately 0.023.

These results confirm the experimental observations reported by [9]. As shown in the dashed branch in Fig. 5.2, as a polypropylene fiber was compressed, it initially buckled toward one of the walls, then switched to a configuration with two turning points. Then, as shown in the dotted branch, upon relaxation, this two-turning point solution was retained past the point at which it originally emerged, rejoining the single-turning point solution via the roughly horizontal curve. The stability results in Fig. 5.2 are consistent with this sort of hysteresis loop: once λ exceeds $15\pi^2$, there is no more one-turning-point stable solution, so we would expect the rod to "snap" to the two-turning-point branch. Similarly, upon relaxation, we would expect to remain on the two-turning-point branch until λ drops below $4\pi^2$, when it would snap to the one-turning-point branch.

Clearly, there are limits to using this idealized 2D rod as a model for the polypropylene fiber.

Upon compression, instead of the hysteretic horizontal jump that the theory would predict, we have a smoother transition via a sloping branch that furthermore reaches higher compression than the theoretical two-turning-point branch. Similarly, upon relaxation, instead of a horizontal jump from two turning points to one, Holmes et al report that the polypropylene fiber passes through an asymmetric two-turning-point state. In fact, there is a branch of such asymmetric states not shown in Fig. 5.2, nearly parallel to the branch of symmetric two-turning point states around $\lambda = 4\pi^2$ (it begins at the bifurcation point suggested by the change in stability at compression 0.023). Neither the branch of symmetric nor asymmetric two-turning point configurations is stable below compression 0.023 in the theoretical model, so it seems there is some perturbation in the physical system that favors the asymmetric states.

5.2. 2D clamped-clamped rods. In Fig. 5.3, we show three bifurcation diagrams for the 2D clamped-clamped problem, for a soft wall with $b = 10^{-3}$, 10^{-4} and 10^{-5}. Once again, as $b \to 0$,

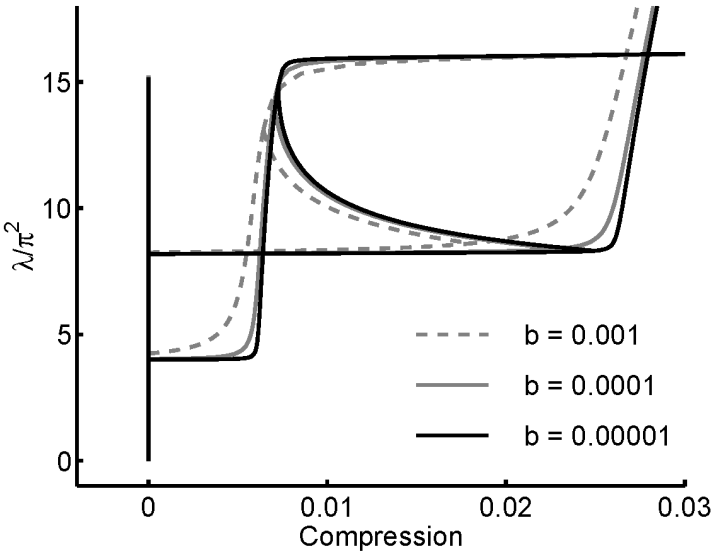

FIG. 5.3. *Convergence as $b \to 0$ of bifurcation diagrams for a 2D rod with clamped-clamped boundary conditions.*

the soft-wall bifurcation diagrams appear to approach a limit, presumably the hard-wall diagram. In Fig. 5.4, we show the soft wall diagram with $b = 10^{-5}$ with stability indicated by linestyle. We see a pattern reminiscent of that seen in the pinned-pinned case, but different in detail. The one-turning-point branch is initially stable but loses stability at a bifurcation point, after which solutions have three turning points. These solutions are initially unstable, but become stabilized by contact with the wall around compression 0.06. The two-turning-point branch is initially unstable, but becomes stable after a bifurcation point, only to become unstable later on (but then, off the edge of the diagram, becoming a branch with stable four-turning-point configurations).

5.3. 3D clamped-clamped rods. We conclude by presenting results for 3D buckling subject to clamped-clamped boundary conditions. In Secs. 5.3.1 and 5.3.2, respectively, we consider rods with

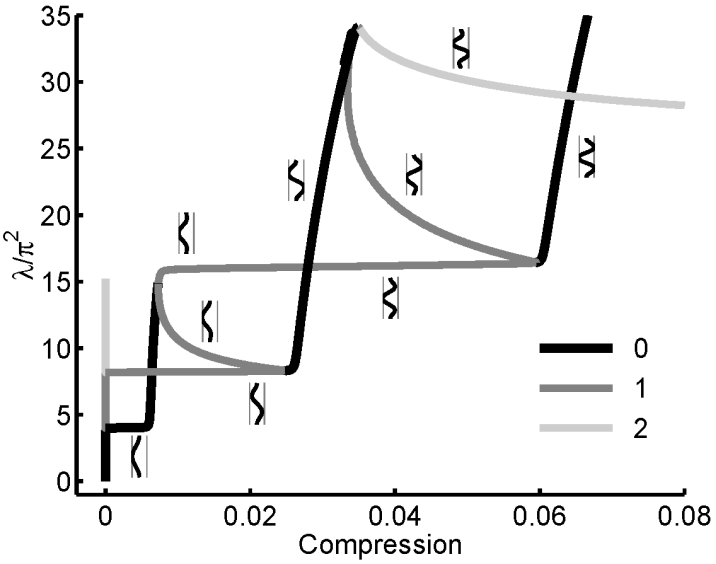

FIG. 5.4. *Bifurcation diagram for a 2D rod with $b = 10^{-5}$ and clamped-clamped boundary conditions, with stability indicated by linestyle.*

circular and elliptical cross-sections, with spacing parameter $a = 0.1$ and strength $b = 10^{-4}$. Some of the most common configurations the rod assumes are portrayed in Fig. 5.5. In the bifurcation diagrams throughout Sec. 5, branches have labels $A1$, $A2$, $B1$, $B2$, C, D, and E corresponding to the configurations in Fig. 5.5.

5.3.1. Rods with circular cross-sections. A rod with a circular cross-section initially buckles in the plane parallel to the soft walls: buckling perpendicular to the walls requires the rod to overcome the wall strength, however slight, while buckling in the y-z plane is free of resistance from the wall. This is illustrated in Fig. 5.6, where branch y (containing configurations parallel to the walls) occurs just before branch x (containing configurations perpendicular to the walls).

On branch y, the rod initially forms a stable one-turning-point bend (index 0) parallel to the walls, but then becomes unstable at a secondary bifurcation point. Table 5.1 displays the value of the compression at this secondary bifurcation point for several values of a and b. The data suggest

Wall spacing parameter (a)	Compression (Wall strength $b = 10^{-4}$)	Compression (Wall strength $b = 10^{-5}$)
0.40	0.8605	0.8605
0.20	0.8606	0.8606
0.10	0.8610	0.8606
0.03	0.8767	0.8622
0.01	1.0000	0.9016

TABLE 5.1
The value of the compression when a rod bending in the y-z plane reaches a secondary bifurcation point, thus becoming unstable.

that for a wall of any strength, this loss of stability occurs for compression 0.86 or higher, at which

point the rod has come in contact with itself (see configuration $B2$ in Fig. 5.5). By this time, a true rod would be subject to self-contact effects not accounted for here.

On branch x, the rod initially forms a one-turning-point bend perpendicular to the wall. These initial configurations are unstable (index 1), and after a significant increase in λ there are secondary bifurcation points, after which the rod becomes more unstable (index 2, 3, 4). Where the dashed gray segment of branch x turns sharply right, the rod forms a three-turning-point configuration perpendicular to the wall. On the first secondary bifurcating branch (branch xy), we have two-turning-point configurations with bends that slide along the wall in opposite directions as seen in configuration E of Fig. 5.5. This branch initially has index 1, but becomes increasingly unstable. So, it seems that the only stable configurations for a rod with circular cross-section in the soft wall model lie on the plane parallel to the walls.

If the wall force at $x = 0$ is sufficiently large (e.g., for a close pair of walls $a = 0.0075$, $b = 10^{-4}$), the behavior on branch x can be slightly different, in that the rod may exhibit multiple turning-points when initially buckling toward the wall (data not shown). However, this can only make the perpendicular configurations more unstable.

Finally, note that Fig. 5.6 includes a portion of the bifurcation diagram in the absence of the wall, to allow comparisons of this and later diagrams with this standard. As one would expect, the no-wall diagram includes a branch of uncompressed solutions containing an infinite family of bifurcation points. Due to the circular symmetry of the no-wall problem, buckling can occur in two dimensions, and hence the index increases by two, at each bifurcation point. The stability of the no-wall diagram is not shown in Fig. 5.6, but by the above argument, the no-wall zero-compression branch has the same 0-2-4-$\cdots$ index pattern seen for the wall problem in Fig. 5.6 (although recall that, for example, the first two bifurcation points in the wall diagram actually have a tiny separation between them, in which the index is one). The first bifurcating branch in the no-wall diagram is identical to the y branch in the wall diagram (with the same index pattern), not surprisingly, since the two wall forces cancel out on the y branch. The no-wall diagram has a secondary bifurcating branch near the wall branch yx, but with a different shape, which is to be expected since these nonplanar solutions do experience the wall when it is present.

5.3.2. Rods with elliptical cross-sections. We now consider rods with elliptical cross-sections whose major axes are parallel to the walls. If the walls are relatively weak, then the first primary bifurcating branch will consist of one-turning-point bends perpendicular to the wall (branch x in Figs. 5.7–5.9) that are initially stable. For higher loads, there will also be a bifurcating branch consisting of bends parallel to the wall (branch y in Figs. 5.7–5.9), but these configurations will be unstable.

For a rod with a slightly elliptical cross-section (e.g., $K_1 = 0.1$, $K_2 = 0.09$ as in Fig. 5.7), the primary bifurcating branches x and y are in close proximity. Branch x almost immediately has a

secondary bifurcating branch, branch xy, which consists of configurations that bend at an angle toward the wall. These configurations look like configuration D in Fig. 5.5, one-turning-point stable bends that exist liminally between the wall and the plane parallel to the wall. The rod seems to find a balance between the force of the wall and its slightly elliptical shape. Intriguingly, these stable bends are nearly identical in shape to the unstable bends in branch y. Thus the bifurcation diagram in Fig. 5.7 displays a stable and an unstable branch that share nearly identical paths.

Looking at a more elliptical rod (e.g., $K_1 = 0.1$, $K_2 = 0.05$ as in Fig, 5.8), the secondary bifurcation point on branch x occurs when the rod is in near contact with the wall. This secondary bifurcating branch, branch xy, contains stable one-turning-point bends that are "folded" along the wall as in configuration C of Fig. 5.5. After the secondary bifurcation point, branch x continues with unstable three-turning-point configurations.

Finally, for an even more extreme ellipse (e.g., $K_1 = 0.1$, $K_2 = 0.02$ as in Fig. 5.9), the formation of three-turning-point configurations occurs closer to emergence of the xy branch of folded bends. Indeed, for the appropriate stiffness parameters, the rod can form a stable three-turning-point configuration perpendicular to the wall before this xy branch, see, e.g., the black segment on branch x in Fig. 5.10.

5.3.3. Conjectures for the hard wall problem. The bifurcation diagrams for walls with $b = 10^{-4}$ and 10^{-5} are nearly identical when a is relatively large and the rod cross-section sufficiently elliptical, e.g., for our diagrams here with $a = 0.1$ and $K_2/K_1 \leq 0.9$. This indicates that the equilibrium configurations and stability analysis have likely already reached their $b \to 0$ limits. This provides inductive evidence that the soft wall problem might be used as an indicator of stability in the hard wall problem, in which a rod buckles into a pair of walls that exert no force for $|x| < a$ and disallow configurations with $|x| > a$. So, for Figs. 5.7–5.10, the bifurcation diagrams for the hard wall should closely resemble those we show for the soft wall.

In cases when the walls are very close, or when the elliptical rod cross-section is nearly circular, the asymptotic approach of the soft wall results to the hard wall results will generally be slower. For example, for a rod with elliptical cross-section with major axis parallel to the hard walls, buckling perpendicular to the walls will occur before buckling parallel to the walls. However, if the soft walls are close to the rod, then the wall strength will tend to reverse this ordering, so that we only get the correct ordering for very small b. Similarly, when the cross-section is nearly circular, the perpendicular branch occurs only slightly before the parallel branch in the hard wall problem, and so it takes only a very small soft wall force to reverse the ordering. Nevertheless, even in these cases, one should still be able to extract a good approximation to the hard wall diagram by taking b sufficiently small in the soft wall problem.

In contrast, the case of a circular rod is somewhat special. For example, when bordered by hard walls, a rod with a circular cross-section is equally likely to buckle in every direction, while when

bordered by soft walls, it can only buckle perpendicular to or parallel to the wall, no matter how small b is. Thus, the circular-rod hard-wall solution set is harder to extract as a simple limit of soft-wall results.

A few conclusions are clear. As in the soft wall model, a rod that bends parallel to a hard wall will form a stable one-turning-point configuration until after it comes in contact with itself, as discussed in Sec. 5.3.1. If the rod buckles toward the wall it would initially form a one-turning-point configuration, but unlike similar configurations in the soft wall model, these configurations would initially be stable (by the circular symmetry of the problem before the wall contact begins). Just as in the soft-wall case, we then expect a secondary bifurcating branch like our soft-wall xy branches (though it is less clear whether configurations will be more like C or D – configurations like D can certainly arise if the initial rod buckling is diagonal to the wall, but their appearance in Fig. 5.7 appears to be due to a balance between the elliptic cross-section and the soft-wall force, an effect that would be absent in the circular-rod hard-wall case). In addition, if we continue past this secondary bifurcation point, the rod should form unstable configurations with three turning points like configuration $A2$ (although, if the walls are sufficiently close, these would presumably emerge as stable solutions before the secondary bifurcation, as we have seen in our soft-wall simulations).

Acknowledgements: R.S.M. was supported by NSF grants DMS-9973258 and DMS-0384739.

REFERENCES

[1] S. S. Antman, *Nonlinear Problems of Elasticity*, Springer-Verlag, 1995.
[2] M. S. Birman and M. Z. Solomajak, *Spectral Theory of Self-Adjoint Operators in a Hilbert Space*, D. Reidel Publishing, 1987.
[3] D. J. Dichmann, Y. W. Li, and J. H. Maddocks, *Hamiltonian formulations and symmetries in rod mechanics*, in Mathematical Approaches to Biomolecular Structure and Dynamics, J. Mesirov, K. Schulten, and D. Sumners, eds., vol. 82, Springer, New York, New York, 1996, pp. 71–113. IMA Volumes in Mathematics and its Applications.
[4] E. H. Dill, *Kirchhoff's theory of rods*, Arch. Hist. Exact Sci., 44 (1992), pp. 1–23.
[5] E. J. Doedel, H. B. Keller, and J. P. Kernévez, *Numerical analysis and control of bifurcation problems, parts I and II*, Int. J. of Bif. and Chaos, 3, 4 (1991), pp. 493–520, 745–772.
[6] G. Domokos, P. Holmes, and B. Royce, *Constrained euler buckling*, J. Nonlinear Sci., 7 (1997), pp. 281–314.
[7] I. M. Gelfand and S. V. Fomin, *Calculus of Variations*, Prentice Hall, Englewood Cliffs, NJ, 1963.
[8] P. Holmes, G. Domokos, and G. Hek, *Euler buckling in a potential field*, J. Nonlinear Sci., 10 (2000), pp. 477–505.
[9] P. Holmes, G. Domokos, J. Schmitt, and I. Szeberényi, *Constrained euler buckling: an interplay of computation and analysis*, Comput. Methods Appl. Mech. Engrg., 170 (1999), pp. 175–207.
[10] T. Kato, *Perturbation Theory for Linear Operators*, Springer-Verlag, 1980.
[11] G. Kirchhoff, *Über das Gleichgewicht und die Bewegung eines unendlich dünnen elastischen Stabes*, Journal für die reine und angewandte Mathematik (Crelle), 56 (1859), pp. 285–313.
[12] A. E. H. Love, *A treatise on the mathematical theory of elasticity*, Dover, 4th ed., 1927.
[13] R. Manning, *Conjugate points revisited and neumann-neumann problems*, preprint.
[14] R. S. Manning, K. A. Rogers, and J. H. Maddocks, *Isoperimetric conjugate points with application to the stability of DNA minicircles*, Proc. R. Soc. London A, 454 (1998), pp. 3047–3074.
[15] M. Morse, *Introduction to Analysis in the Large*, Institute for Advanced Study, Princeton, New Jersey, 1951.
[16] A. W. Naylor and G. R. Sell, *Linear Operator Theory in Engineering and Science*, Springer-Verlag, New York, 1982.
[17] M. Renardy and R. Rogers, *An Introduction to Partial Differential Equations*, Springer-Verlag, New York, 1993.
[18] B. Roman and A. Pocheau, *Buckling cascade of thin plates: Forms, constraints and similarity*, Europhys. Lett., 46 (1999), pp. 602–608.
[19] L. S. Schulman, *Techniques and Applications of Path Integration*, Wiley, New York, 1981.
[20] G. H. M. van der Heijden, *The static deformation of a twisted elastic rod constrained to lie on a cylinder*, Proc. R. Soc. Lond. A, 457 (2001), pp. 695–715.
[21] A. Weinstein and W. Stenger, *Methods of Intermediate Problems for Eigenvalues: Theory and Ramifications*, Academic Press, New York, 1972.

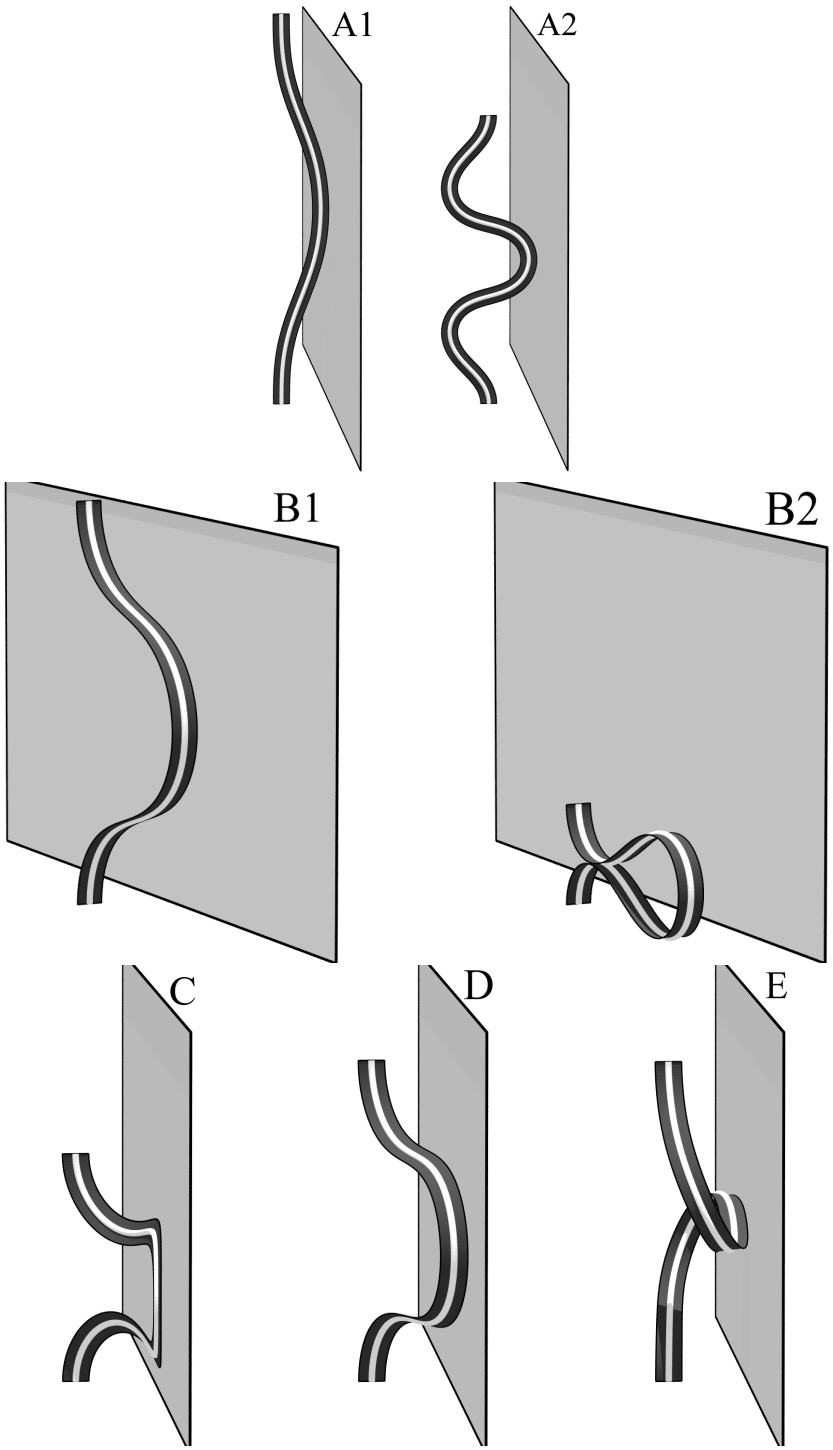

FIG. 5.5. *Common equilibrium rod configurations (only one wall shown). Figures A*1 *and A*2 *show bending perpendicular to, and nearly touching, a wall: the rod initially forms a one-turning-point configuration but buckles again forming a configuration with three turning points. Figures B*1 *and B*2 *represent the progression of the rod bending in the y-z plane parallel to the walls. Figure C shows a single bend sliding along the wall. Figure D shows a configuration bending at an angle toward the wall. Figure E shows a rod with two bends sliding along the wall in opposite directions.*

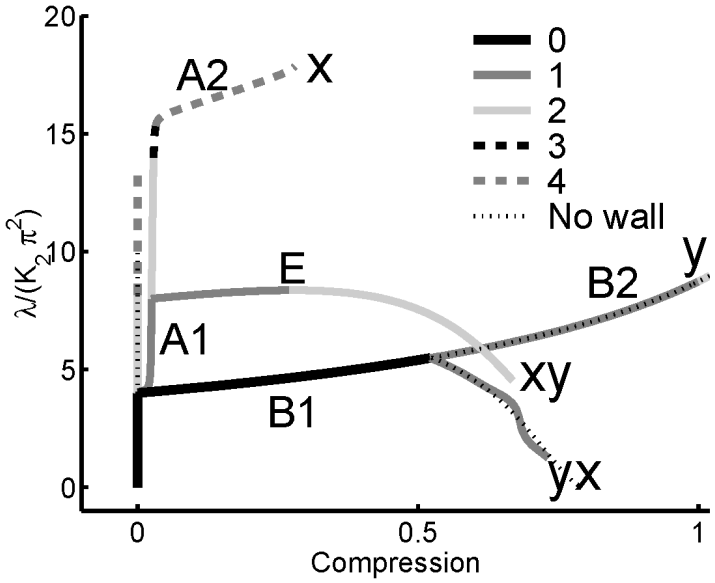

FIG. 5.6. *Bifurcation diagram for a rod with circular cross-section ($K_1 = K_2 = 0.1, K_3 = 0.06$), bordered by walls with spacing parameter $a = 0.1$ and strength $b = 10^{-4}$. The labels $A1$, $A2$, $B1$, $B2$, and E refer to the corresponding configurations in Fig. 5.5.*

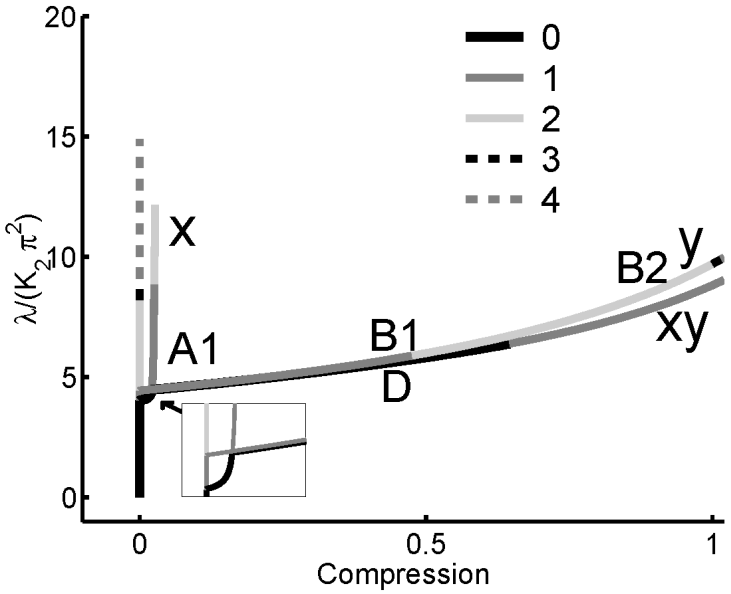

FIG. 5.7. *Bifurcation diagram for a rod with a slightly elliptical cross-section ($K_1 = 0.1, K_2 = 0.09, K_3 = 0.06$), bordered by walls with $a = 0.1$ and $b = 10^{-4}$. Two branches follow nearly identical paths: the stable branch corresponds to configurations that exist liminally between the wall and the y-z plane; and the unstable branch corresponds to configurations in the y-z plane.*

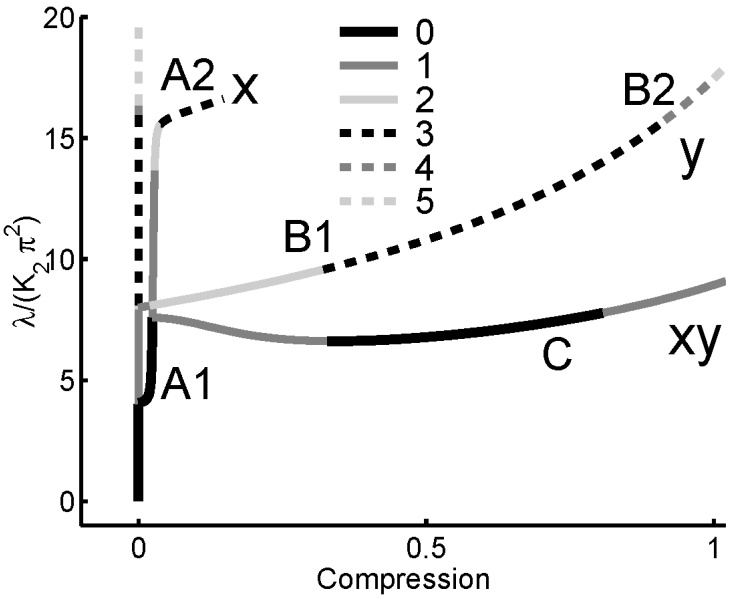

FIG. 5.8. *Bifurcation diagram for a rod with a moderately elliptical cross-section ($K_1 = 0.1, K_2 = 0.05, K_3 = 0.06$), bordered by walls with $a = 0.1$ and $b = 10^{-4}$.*

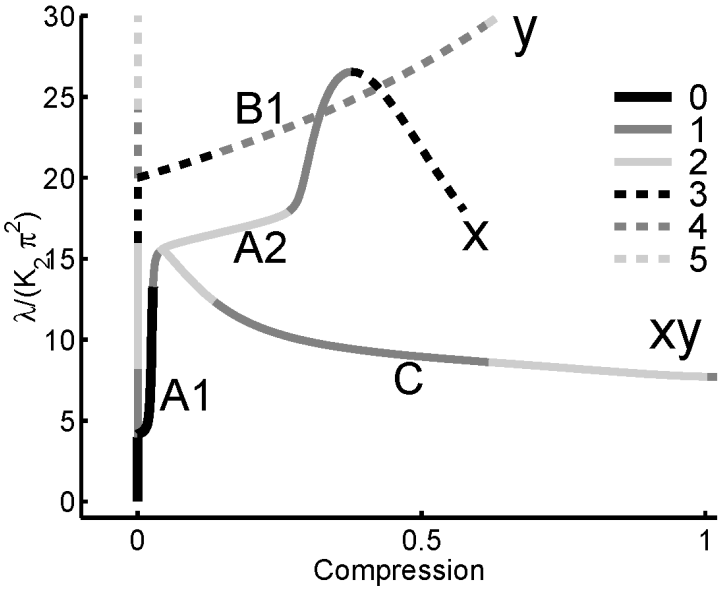

FIG. 5.9. *Bifurcation diagram for a rod with an extremely elliptical cross-section ($K_1 = 0.1, K_2 = 0.02, K_3 = 0.06$), bordered by walls with $a = 0.1$ and $b = 10^{-4}$.*

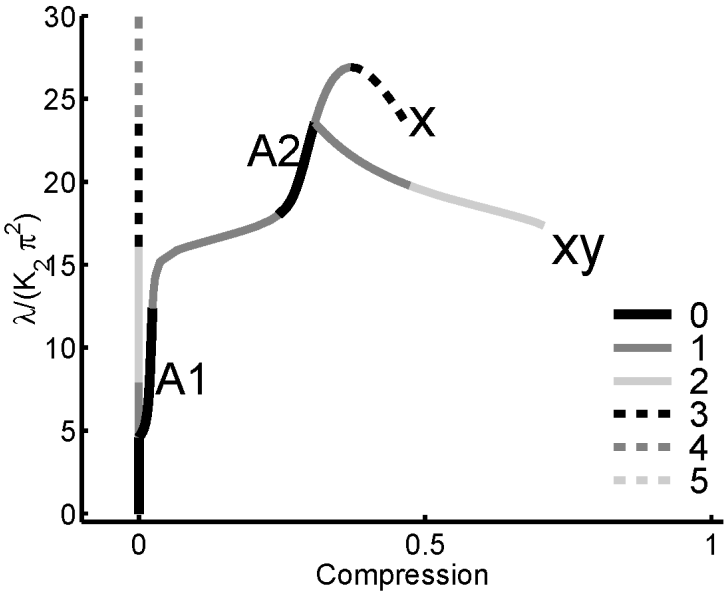

FIG. 5.10. *Bifurcation diagram for a rod with sufficiently elliptical cross-section ($K_1 = 0.1, K_2 = 0.005, K_3 = 0.05$) that there are stable configurations of the shape A2 from Fig. 5.5. Wall parameters are $a = 0.1, b = 10^{-4}$.*